# Computational insights into the underlying mechanism of zinc ion-specificity of the fluorescent probe, BDA-1

Quyan Su [a], Jia Han [b], Haili Yu [a], Xiaoguo Zhou [a,b,*], Shilin Liu [a,b,*]

[a] Department of Chemical Physics, University of Science and Technology of China, Hefei, 230026, China
[b] Hefei National Research Center for Physical Sciences at the Microscale, University of Science and Technology of China, Hefei, 230026, China

HIGHLIGHTS

- Internal conversion suppresses the fluorescence of BDA-1 rather than photoinduced electron transfer.
- Adding Zn or Cd ions causes photoinduced electron transfer in [M:BDA-1$_{-H+}$]$^+$ (M = Zn, Cd) complexes upon photoexcitation.
- Compared to the suppressed radiation from [Cd:BDA-1$_{-H+}$]$^+$ in the S1 state, [Zn:BDA-1$_{-H+}$]$^+$ has considerable oscillator strength.

GRAPHICAL ABSTRACT
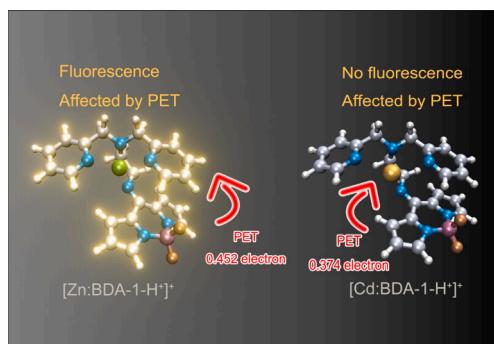
ARTICLE INFO

ABSTRACT

Ion specificity is crucial for developing fluorescence probes. Using a recently reported optical sensor (BDA-1) of Zn^{2+} as a representative, we carried out extensive quantum chemical calculations on its photophysical properties using density function theory. According to the calculated optimized geometries, excitation energies and transition oscillator strengths, the weak fluorescence of BDA-1 observed in experiments is attributed to the suppression of fluorescence emission by efficient internal conversion, rather than the previously proposed photoinduced electron transfer (PET) mechanism. With the addition of Zn^{2+} or Cd^{2+} ions, the tetradentate chelates [M:BDA-1$_{-H+}$]$^+$ (M=Zn, Cd) are produced. According to frontier molecular orbital and interfragment charge transfer analyses of these complexes, PET is preferentially confirmed to occur upon photo-excitation. Notably, as one coordination bond in the excited [Cd:BDA-1$_{-H+}$]$^+$ complex is significantly weakened in comparison to that of [Zn:BDA-1$_{-H+}$]$^+$, their molecular orbital compositions in the S$_1$ state are completely different. As a result, absorption and radiation transitions of [Zn:BDA-1$_{-H+}$]$^+$ both have considerable oscillator strength, while fluorescence radiation from the excited [Cd:BDA-1$_{-H+}$]$^+$ is doubly suppressed. This difference causes that the fluorescence intensity of BDA-1 is sensitive to the addition of metal ions, and exhibits the zinc ion-specificity.

* Corresponding authors.
  E-mail addresses: xzhou@ustc.edu.cn (X. Zhou), slliu@ustc.edu.cn (S. Liu).

1. Introduction

Transition metal ions play an important role in many life activities. Among the transition metal ions, Zn^{2+} ion has the second abundance in the human body and plays a significant role in fundamental physiological processes as cofactors for metalloproteins and regulators of enzyme function in neural signal transmission and gene expression [1,2]. Its appropriate concentration is vital for maintaining health of living organisms, while the opposite often leads to serious diseases, such as Alzheimer's, Parkinson's disease, amyotrophic lateral sclerosis and epilepsy [3]. Therefore, accurate measurement of the Zn^{2+} concentration in biological systems is extremely critical to understanding the pathogenesis of the relevant diseases [4].

Many analytical techniques have been applied for detecting metal ions like Zn^{2+} at low concentrations, e.g. electrochemical sensors, UV–visible absorption spectroscopy, flame atomic absorption spectroscopy, microwave plasma-atomic emission spectroscopy, and fluorescence emission spectroscopy [5]. Among these experimental approaches, fluorescence spectroscopy assay using optical sensors has impressive advantages of good selectivity, high sensitivity, and fast response speed [6]. Recent advancements in fluorescent probes have significantly improved non-invasive imaging for detecting mobile metal ions in living specimens, [7] with better selectivity, lower detection limits, [8] and have resolved the issue of false negative backgrounds caused by fluorescence bleaching [9]. Some fluorescent sensors based on various fluorophores for Zn^{2+} detection have been developed [10]. With the addition of Zn^{2+} ions, fluorescence intensities of these optical sensors are significantly enhanced, via photo-induced electron transfer (PET), [11] intramolecular charge transfer (ICT), [12] excited-state intramolecular proton transfer (ESIPT), [13] or aggregation-induced emission (AIE) [14] mechanisms. However, there are still some grand challenges, such as complex synthesis, susceptibility to biological environments, certain biological toxicity, and limitations to *in vitro* and living cell imaging of Zn^{2+}. Besides, the Zn^{2+} detection often faces interferences from Cd^{2+}, [15,16] because both of them belong to the same group in the periodic table and have similar electronic configuration of nd^{10}.

Recently, a novel Zn^{2+}-specific fluorescent probe for *in vivo* detection in zebrafish, N-((BODIPY-8-yl)methyl)-N-(pyridin-2-yl)pyridin-2-amine (BDA-1), has been reported [17]. As a typical tetradentate chelating ligand, it provides four coordination sites to bind a metal ion upon deprotonation, producing the complex ion of $[M:BDA-1_{-H+}]^+$, as shown in Scheme 1. Notably, this probe demonstrates specific fluorescence enhancement for Zn^{2+} ions, in comparison to other competitive metal ions like Cd^{2+}. With the absence of Zn^{2+} ions, the fluorescence quantum yield of BDA-1 was determined to be only 0.01, while it was significantly improved to 0.14 with the addition of Zn^{2+}. Based on the DFT-optimized structures of the BDA-1 monomer and $[Zn:BDA-1_{-H+}]^+$ complex in ground state, as well as frontier molecular orbital (MO) analyses, the authors postulated that this fluorescence-enhanced effect stemmed from the fact that the PET process of the monomer was inhibited in the complexes [17]. However, it is worth noting that the influence of
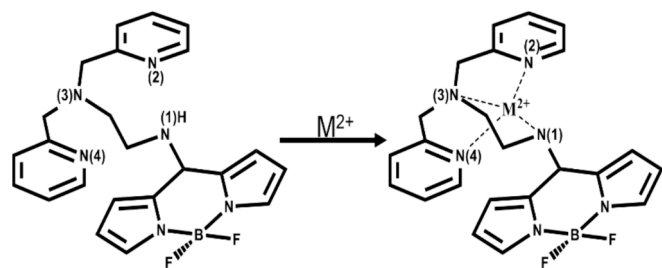
geometric changes between absorption and fluorescence emission processes did not take into account there, which usually led to an exchange of MO energy orders. Therefore, with the absence of MO analyses at optimized geometries of electronically excited states, the PET action mechanism of BDA-1 for Zn^{2+} detection is arbitrary and questionable. It gave us the initial motivation to apply theoretical calculations to thoroughly explain the fluorescence-enhanced mechanisms involved.

Another important aim of the present investigation is to unravel the nature of this probe's specific response to zinc ions. Thus, quantum chemical calculations have been performed on the complexes consisting of BDA-1 and Zn^{2+}/Cd^{2+}, to obtain optimized geometries in ground and excited states, frontier MO analyses, photo-absorption and fluorescence emission properties. By comparing two complex ions, we propose a comprehensive interpretation for the Zn^{2+} specificity of the BDA-1 probe.

2. Computational details

Considering there might be various isomers for the $[M:BDA-1_{-H+}]^+$ (M=Zn^{2+}, Cd^{2+}) complex, a large number of initial molecular geometries of the BDA-1 monomer and the complex ions (total charge is + 1 after deprotonation) were generated using Gentor program [18]. Preliminary screening was carried out at the semi-empirical quantum mechanical method, GFN2-xTB, [19] using the xtb42 [20] program through Moclus [18]. Further quantum chemical computations were performed using the Gaussian 16 software package [21]. Density functional theory (DFT) [22] and time-dependent density functional theory (TDDFT) [23] were used here to optimize geometries of the monomer and complexes in ground and excited electronic states, respectively, at the B3LYP [24] level. The 6-31G(d) [25] and LanL2DZ [26] basis sets were applied for main group elements and transition metals, respectively. Using the optimized geometries, harmonic vibrational frequencies were calculated at the same level, to ensure no imaginary frequencies for all minima and to calculate zero-point energy corrections. The DFT-D3 method was further applied to make dispersion corrections, using Grimme [27]. Solvent effect was also considered in aqueous solutions using the conductor-like polarizable continuum model (PCM) [28]. Moreover, to understand coordination interactions clearly, Multiwfn 3.8 [29] was conducted to plot localized orbital locator (LOL) maps [30] and perform Mayer bond-order [31] analyses. In addition, to quantitatively assess electron-transfer percentage probably involved in photo-excitation and energy decay processes, interfragment charge transfer (IFCT) analyses [29] were performed too.

3. Results and discussion

3.1. Absorption and emission properties of BDA-1

Fig. 1 shows the optimized geometries of the BDA-1 monomer in three lowest electronic states, S_0, S_1 and S_2. Notably, the present ground-state structure is different from that proposed by Chen et al. [17] (Figure S1 of the supporting information), which is unstable at the present and M06-2X/6-31G(d) and ωB97XD/6-31G(d) levels of theory (Table S2). The similar optimized geometry is also obtained at two higher levels, M06-2X/6-31G(d) and ωB97XD/6-31G(d), indicating the reliability of the current structure calculations (Figure S3). As shown in Fig. 1, the dihedral angle D_1 is significantly increased from 45.6° in S_0 to 91.6° in S_1, while this angle is slightly changed when the molecule is excited to the S_2 state.

Using the optimized S_0 geometry, absorption properties of BDA-1 were calculated and summarized in Table 1. In previous experiment, [17] the first absorption band of BDA-1 was observed in the range of 350–420 nm with a peak at 390 nm. As shown in the calculated results of Table 1, the $S_0 \rightarrow S_1$ transition is very weak (transition oscillator strength f is only 0.0080) and its excitation energy ΔE is only 3.01 eV (412 nm), whilst the $S_0 \rightarrow S_2$ transition is much stronger with $f = 0.3106$ and
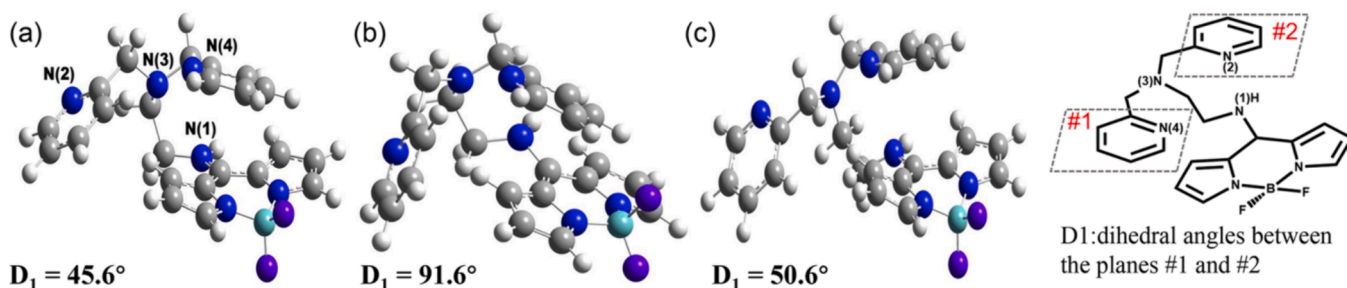

Scheme 1. Molecular structures of the BDA-1 ligand and the metal ion:BDA-1 complex, $[Zn:BDA-1_{-H+}]^+$.

Fig. 1. Optimized geometries of BDA-1 in the ground state (S_0) and two lowest excited states (S_1 and S_2), respectively.

Table 1
Properties of absorption (abs.) and fluorescence (fl.) transitions of BDA-1, where MOs involved in transition and the corresponding predominant CI coefficients are shown as well. BDP represents the BODIPY unit.

transition	λ/nm (ΔE/eV)	f	MO assignment [a]	coeff.
$S_0 \to S_1$ (abs.)	412 (3.01)	0.0080	n (N) → π* (BDP)	0.6707
$S_0 \to S_2$ (abs.)	367 (3.38)	0.3106	π (BDP) → π* (BDP)	0.6633
$S_1 \to S_0$ (fl.)	700 (1.77)	0.0009	n (N) → π* (BDP)	0.7068
$S_2 \to S_0$ (fl.)	426 (2.91)	0.4716	π (BDP) → π* (BDP)	0.7036

[a] N is the nitrogen atom of the tertiary amine, N(3), and BDP represents the bodipy unit.

ΔE=3.38 eV (367 nm). Such large changes of the f values can be explained by MO analyses. At the S_0 geometry, HOMO, HOMO-1 and LUMO are located on the non-bonding oribital (n) of the N(3) atom, the π and π* orbitals of the bodipy unit (BDP), respetively. Thus, the $S_0 \to S_1$ and $S_0 \to S_2$ transitions are mainly contributed by nπ* and ππ* components, respectively. As the former corresponds to the formation of a charge-seperated state, its transition intensity is reasonably weak, in line with the experimental and calculated results. Based on these knowledges, the experimental absorption at ∼ 390 nm may be exclusively attributed to the $S_0 \to S_2$ transition.

It is well known that fast intramolecular vibrational redistribution (IVR) usually occurs prior to radiation decay for polyatomic molecules upon Franck-Condon excitation to electronically excited states, and hence fluorescence emission properties of BDA-1 should be considered at the optimized structures of corresponding excited states. Using the optimized geometries of S_1 and S_2 in Fig. 1, we conducted comprehensive calculations to identify emission energies, oscillator strengths, and predominant MOs involved in related radiative transitions, and summarized the results in Table 1 too.

At the S_1 optimzied geometry, the energy gap between the S_0 and S_1 states is dramatically reduced energy state (ΔE=1.77 eV), in comparison to 3.01 eV in absorption. However, its nπ* feature remains unchanged according to the same HOMO and LUMO. Therefore, the S_1 state still exhibits an optically "dark" property with a very low f of 0.0009. In contrast, the transition of $S_0 \to S_2$ at the S_2 optimized geometry is slightly changed from the one in absorption process. An enhanced f value of 0.4716 and the ππ* feature are obtained. Moreover, the excitation energy is moderately reduced to 2.91 eV (426 nm) owing to IVR process, which greatly agrees with the fluorescence emission wavelength range (with a peak of 450 nm) observed in experiments [17]. Notably, the experimental fluorescence was very weak (quantum yield Φ_{FL}=0.01) and opposite to such a large f value in calculations. This contradiction strongly implies that non-radiative decay pathways of the S_2 state, such as internal conversion (IC), might play an important role, competing with fluorescence emission.

According to the energy gap law, we roughly estimated the fluorescence rate constant (k_{FL}) and the IC rate constant (k_{IC}) using the formula (1) and (2), [32]

$$k_{FL} = f_{FL} \bullet \Delta E^2 / 1.499 \tag{1}$$

$$\log\left(k_{IC}/s^{-1}\right) \approx 12 - 2 \bullet \frac{\Delta E}{hc} \tag{2}$$

where f_{FL} represents oscillator strength of radiative emission at the corresponding optimized geometry with the unit of cm^{-1}, h is Planck constant, c is the light speed in vacuum, and ΔE is the energy gap between initial and final states. Using the calculated data in Table 1, the k_{FL} value of $S_2 \to S_0$ is determined to be 1.86×10^8 s^{-1} and k_{IC} of $S_2 \to S_1$ equals to 3.48×10^{10} s^{-1}, respectively. In addition, the k_{IC} of $S_2 \to S_0$ is calculated to be 8.62×10^6 s^{-1}, much slower than the fluorescence rate. Therefore, the IC process of $S_2 \to S_1$ is far more favorable relative to fluorescence emission. In other words, the most predominant energy decay of BDA-1 in the S_2 state is via IC to the dark state, S_1, followed by non-radiative relaxation such as collision to ground state, rather than fluorescence emission, as indicated in Fig. 2. Additionally, considering that no significant changes in their molecular orbital properties occur, there is no obvious crossing between potential energy surfaces of the S_1 and S_2 states, and hence the experimental phenomenon of fluorescence suppression cannot be attributed to the PET mechanism, as proposed previously [17].

3.2. Coordination bonding features of metal ion-ligand complexes

With the action of tetradentate chelating interaction, deprotonated BDA-1 can easily bind to a Zn^{2+} or Cd^{2+} ion. Fig. 3 displays their optimized geometries in the ground (S_0) and the lowest excited (S_1) states. Notably, in order to form the tetradentate chelates, the dihedral angle D_1 of BDA-1 ligand is significantly increased from 45.6° to 171.8° in [Zn:BDA-1$_{-H+}$]$^+$ and 163.5° in [Cd:BDA-1$_{-H+}$]$^+$ in their own ground states, leading to a convergence of the two pyridine rings to parallelism. Moreover, four coordination bond lengths in [Zn:BDA-1$_{-H+}$]$^+$ and [Cd:
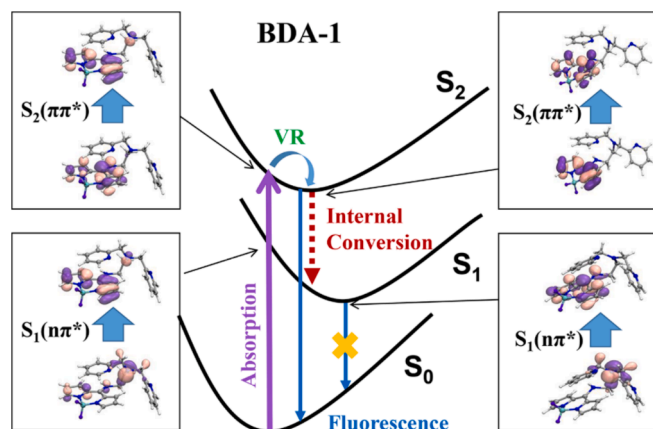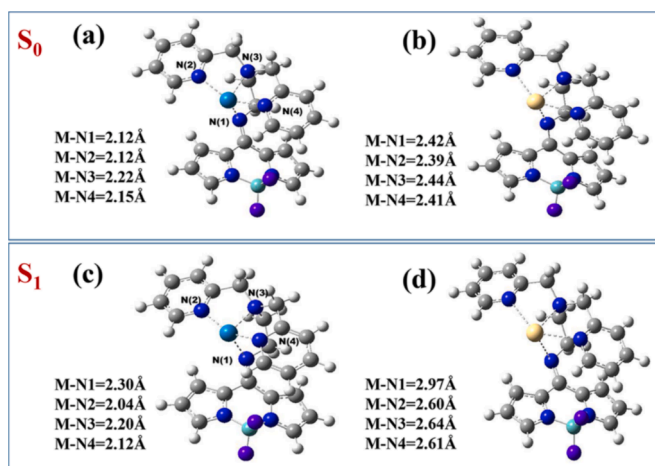

Fig. 2. Absorption and energy decay processes of BDA-1 after photoexcitation to the S_2 state, where the left panels show MOs in the $S_0 \to S_1$ and $S_0 \to S_2$ transitions at the S_0 optimized geometry, and the right one listed the results at the own optimized geometries of S_1 and S_2.
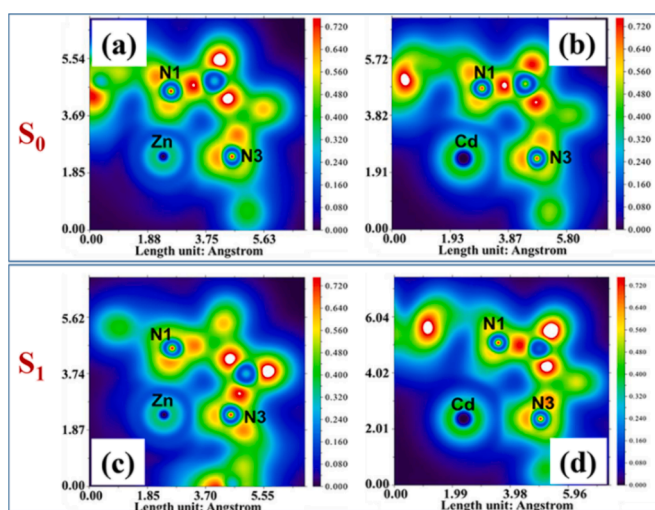
Fig. 3. Optimized geometries of metal ion-ligand complexes in the S_0 and S_1 states, (a) and (c) for $[Zn:BDA-1_{-H+}]^+$, (b) and (d) for $[Cd:BDA-1_{-H+}]^+$.

BDA-$1_{-H+}]^+$ are 2.12 and 2.42 Å for M−N(1), 2.12 and 2.39 Å for M−N(2), 2.22 and 2.44 Å for M−N(3), 2.15 and 2.41 Å for M−N(4), respectively. Obviously, with the increase of the effective ionic radius of metal ion, coordination bond lengths increase synchronously.

Using these optimized ground-state geometries, electron density topological surface shown as LOL maps, as well as Mayer bond orders, were analyzed to identify coordination bonding interactions. Fig. 4a and 4b display the calculated LOL maps, and Table 2 summarizes the results of Mayer bond orders. For the two $[M:BDA-1_{-H+}]^+$ complexes, lone-pair electrons of the nitrogen atom are both located in the coordination direction owing to the ion attraction and predominately remain on the nitrogen atom side, verifying covalent properties of the forming ion-ligand coordination bonds and no charge transfer between metal ion and ligand. Moreover, Mayer bond orders of the ground-state [Zn:BDA-$1_{-H+}]^+$ and [Cd:BDA-$1_{-H+}]^+$ are all in the range of 0.22 and 0.38, in line with the fact that lone-pair electrons of nitrogen atoms gravitating towards the metal ions (as shown in Fig. 4).

However, the interaction between metal ion and ligand is visibly changed in their excited states. In the four coordination bond lengths of [Zn:BDA-$1_{-H+}]^+$ in the S_1 state, the coordination bond length of Zn-N(1) is slightly elongated to 2.30 Å, while the other coordination bond lengths generally remain, as shown in Fig. 3c. As a result, only minor

Fig. 4. Electron density topological surfaces of metal ion-ligand complexes in the S_0 and S_1 states, (a) and (c) for $[Zn:BDA-1_{-H+}]^+$, (b) and (d) for $[Cd:BDA-1_{-H+}]^+$.

Table 2
Mayer bond orders between metal ion and nitrogen atoms in metal ion complexes in ground and lowest excited states.

species	state	M^{2+}-N(1)	M^{2+}-N(2)	M^{2+}-N(3)	M^{2+}-N(4)
$[Zn:BDA-1_{-H+}]^+$	S_0	0.384	0.332	0.244	0.336
$[Zn:BDA-1_{-H+}]^+$	S_1	0.338	0.329	0.251	0.355
$[Cd:BDA-1_{-H+}]^+$	S_0	0.308	0.302	0.218	0.291
$[Cd:BDA-1_{-H+}]^+$	S_1	0.153	0.267	0.223	0.272

decrease is found with the corresponding Mayer bond order. In contrast, in [Cd:BDA-$1_{-H+}]^+$ in the S_1 state, the distance between the Cd and N(1) atoms is significantly increased to 2.97 Å, and the other three coordination bond lengths are also elongated in some extent (Fig. 3d). These remarkably weakened interactions directly lead to the reductions of Mayer bond orders. Notably, Mayer bond order of the Cd-N(1) coordination bond is only 0.153, implying a very weak coordination interaction between the metal ion and the N(1) atom. Actually, this difference of coordination interaction between the excited [Zn:BDA-$1_{-H+}]^+$ and [Cd:BDA-$1_{-H+}]^+$ complexes might cause a change in the energy sequence of frontier molecular orbitals.

3.3. Absorption and emission properties of $[Zn:BDA-1_{-H+}]^+$

As indicated in the previous experiment, [17] the first absorption peak of [Zn:BDA-$1_{-H+}]^+$ was observed at 397 nm, while the maximum fluorescence intensity was located at 450 nm. It is worth noting that both absorption and fluorescence peak positions were close to those of BDA-1 monomer, but the observed fluorescence intensity at 450 nm was significantly increased by 16 times (Φ_{FL}=0.14). To explore the underlying causes of this fluorescence enhancement, properties of absorption and fluorescence transitions of the [Zn:BDA-$1_{-H+}]^+$ complex were calculated, and major results were summarized in Table 3.

Owing to strong tetradentate chelating interactions, energy sequence and predominant components of frontier MOs in the complexes are significantly changed, resulting in the variation of the corresponding transition energies. For instance, non-bonding orbitals on nitrogen atoms disappear due to the formation of coordination bonds between Zn^{2+} and ligand, and thus the original transition of n(N) → π*(BDP) in the BDA-1 monomer does not exist in complex. Instead, the first absorption band ($S_0 \rightarrow S_1$) of the [Zn:BDA-$1_{-H+}]^+$ complex is located at 368 nm in our calculations, which is generally consistent with the experimental peak position. This band has a sizable transition oscillator

Table 3
Properties of absorption (abs.) and fluorescence (fl.) transitions of the [Zn:BDA-$1_{-H+}]^+$ and [Cd:BDA-$1_{-H+}]^+$ complexes, where MOs involved in transition and the corresponding predominant CI coefficients are shown as well. BDP is the BODIPY unit, and PY is the pyridyl ring.

species	transition	λ/nm (ΔE/eV)	f	MO assignment	coeff.
[Zn:BDA-$1_{-H+}]^+$	$S_0 \rightarrow S_1$ (abs.)	368 (3.37)	0.1835	π (BDP) → π* (BDP) + π* (PY)	0.6982
	$S_0 \rightarrow S_2$ (abs.)	341 (3.64)	0.0175	π (BDP) → π* (PY)	0.6877
	$S_0 \rightarrow S_3$ (abs.)	336 (3.69)	0.1124	π (BDP) → π* (BDP) + π* (PY)	0.6406
	$S_0 \leftarrow S_1$ (fl.)	478 (2.59)	0.0814	π (BDP) ← π* (PY)	0.6982
[Cd:BDA-$1_{-H+}]^+$	$S_0 \rightarrow S_1$ (abs.)	369 (3.36)	0.1384	π (BDP) → π* (BDP) + π* (PY)	0.6834
	$S_0 \rightarrow S_2$ (abs.)	339 (3.66)	0.1023	π (BDP) → π* (BDP) + π* (PY)	0.6449
	$S_0 \rightarrow S_3$ (abs.)	336 (3.69)	0.0114	π (BDP) → π* (PY)	0.6730
	$S_0 \leftarrow S_1$ (fl.)	510 (2.43)	0.0096	π (BDP) ← n (Cd)	0.7026

strength ($f = 0.1835$), because it is attributed to the transition from the π orbitals of BODIPY unit to the π^* orbitals in the π-π stacking region consisting of BODIPY and pyridine ring. Notably, this transition slightly differs from the corresponding one of BDA-1 monomer (the $S_0 \rightarrow S_2$ transition in Table 1), since the latter is almost completely located at the BODIPY unit. This delocalization in the complex unsurprisingly attenuates the oscillator strength. Moreover, acompanyed by vibrational relaxation and geometric change to its optimzied structure of the excited $[Zn:BDA-1_{-H+}]^+$ in the S_1 state, the dominant component of the π^* orbital is slightly changed to the local π^* orbital of one pyridyl ring. Therefore, although the radiative transition of $S_0 \leftarrow S_1$ maintains the $\pi\pi^*$ characteristic, the S_1 state indeed becomes a partially charge-separated state in its optimized geometry, in line with its relatively weak transition strength ($f = 0.0814$).

Fig. 5 presents a schematic diagram of the excited energy decay process of $[Zn:BDA-1_{-H+}]^+$ in the S_1 state. Once the excited complex is prepared with the Franck-Condon excitation, a typical donor-excited PET (so-called "d-PET") process occurs with fast vibrational relaxation on the adiabatic potential energy surface of the S_1 state, in which MO analyses indicate the presence of the electron transfer from the mixed π^* orbital of the BODIPY unit and pyridine ring to the π^* orbital of isolated pyridine ring. To further validate the PET contributions, the amount of transferred electrons was determined by the IFCT calculations. For simplicity, we divided a complex molecule into four candidate fragments: BODIPY (BDP), N,N-Dimethylethylenediamine (DME), pyridyl rings (PY) and metal ion center (M). Table 4 summarizes the calculated IFCT results at the optimized geometries of the S_0 and S_1 states, respectively.

In the BDA-1 monomer, the amount of net transferred electrons to form the S_1 state is determined to be 0.721 at the S_0 geometry, which predominantly occurs from the BODIPY to DME units. Such a large amount greatly agrees with its $n\pi^*$ characteristics. In the S_2 formation, IFCT calculations show that only a small number of electrons are transferred, as shown in Table 4. Almost equal amounts of electrons are transferred in the radiative decay of the excited BDA-1 in the S_1 and S_2 states, respectively. Therefore, S_1 is a typical charge-separated state indeed, while the S_2 state is electron-localized with large optical-allowed oscillator strength. However, due to the competition by the more favorable IC of $S_2 \rightarrow S_1$, only weak fluorescence was observed in experiments, [17] as discussed above.

Completely different electron-transfer processes occur in the metal ion-ligand complex, $[Zn:BDA-1_{-H+}]^+$. As indicated in Table 4, 0.303 electrons is transferred from the BODIPY unit to the PY fragment during the $S_0 \rightarrow S_1$ transition process, indicating the characteristics of localized excitation with a minor charge-transfer state. Notably, this amount is remarkably increased to 0.755 during the radiative process of $S_1 \rightarrow S_0$, in great agreement with the PET mechanism. Interestingly, although this PET process can significantly weaken its fluorescence emission ability, the overall fluorescence quantum yield is efficiently improved due to suppression of the IC contributions, in comparison to the BDA-1 itself.
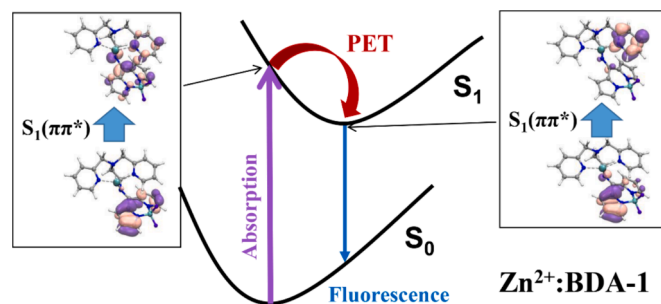
3.4. Absorption and emission properties of $[Cd:BDA-1_{-H+}]^+$

To in-depth understand the zinc ion-specific effect of the BDA-1 fluorescence probe, its interaction with Cd^{2+} ions and photophysical dynamic properties are necessary as a comparison. As mentioned above, Mayer bond order of the Cd-N(1) coordination bond is significantly reduced in the excited $[Cd:BDA-1_{-H+}]^+$ complex, and the MO energy sequence may be changed as a result. As indicated in our calculations (Table 3), the first absorption band of $[Cd:BDA-1_{-H+}]^+$ is located at 369 nm with a moderate oscillator strength ($f = 0.1384$), in line with the experimental peak. The MOs involved in this transition ($S_0 \rightarrow S_1$) is similar to those in the $[Zn:BDA-1_{-H+}]^+$ system, which are contributed by the transition from the π orbitals of BODIPY unit to the π^* orbitals in the π-π stacking region consisting of BODIPY, pyridine ring and lone-pair electrons of nitrogen atom (N1) on tertiary amine (i.e. DMA). The IFCT calculations at the S_0 geometry show that 0.215 or 0.198 electrons are transferred from the BODIPY unit to the PY fragment or the Cd^{2+} ion at the center, respectively (Table 4). These results of IFCT and MO analyses greatly agree with its slightly weaker absorption than that of the $[Zn:BDA-1_{-H+}]^+$ system, as the transition in $[Cd:BDA-1_{-H+}]^+$ exhibits more delocalization properties.

Along with geometric changes and vibrational relaxation on the adiabatic potential energy surface of the S_1 state, MO compositions and orbital energies are significantly changed. As shown in Table 3, the $S_0 \leftarrow S_1$ radiative transition at the S_1 optimized geometry is predominantly composed of the MO transition from the π orbitals on BODIPY to a non-bonding orbital contributed by the d orbital of metal ion, i.e. a ligand-to-metal charge transfer (LMCT) process. We know, a LMCT state usually has the lower excitation energy than a locally excited state, as well as small oscillator strength. Thus, the emission wavelength of $S_0 \leftarrow S_1$ is red-shifted to 513 nm, and the corresponding f value is close to zero (0.0096 in Table 3), which generally agrees with the experimental data.

Based on the discussions above, the overall excited energy decay process of $[Cd:BDA-1_{-H+}]^+$ in the S_1 state is shown in Fig. 6. Due to the strong interaction between metal ion and ligand after Franck-Condon excitation to the S_1 state, 0.572 electrons is transferred from the BODIPY unit to the central Cd^{2+} ion, together with 0.156 electron-transfer from the DME fragment to the metal ion, as indicated in Table 4 of IFCT analyses. In other words, a d-PET process occurs during vibrational relaxation on the S_1 state, where the predominant MO component is changed from the hybridized π^* orbitals to the d orbital of Cd^{2+} ion. As a result, the S_1 state of the $[Cd:BDA-1_{-H+}]^+$ metal–ligand complex has very limited fluorescence emission ability as a dark state.

It is worth noting that different products are formed in the d-PET process for the $[Zn:BDA-1_{-H+}]^+$ or $[Cd:BDA-1_{-H+}]^+$ complexes in the S_1 state, leading to significantly different performances in the experimentally observed fluorescence intensity. As mentioned above, although the d-PET process can weaken fluorescence emission of S_1 to some extent, the forming charge-separated state of $[Zn:BDA-1_{-H+}]^+$ still exhibits considerable radiative ability ($f = 0.0814$) due to the partially overlapping of MOs. In contrast, the S_1 state of $[Cd:BDA-1_{-H+}]^+$ as a typical LMCT state is optically "dark". Thus, the fluorescence radiation in the $[Cd:BDA-1_{-H+}]^+$ complex is doubly suppressed.

4. Conclusions

In the current works, we conducted extensive DFT/TD-DFT calculations on photophysical properties of a zinc ion-specific probe, BDA-1. According to the calculated excitation energies and transition oscillator strengths, the S_2 state of BDA-1 is suggested to dominantly contribute the first absorption band observed in the previous experiment [17]. The excited BDA-1 prefers to decay to the lower-lying electronic state (S_1) via efficient internal conversion, rather than fluorescence emission. Considering that the S_1 is an $n\pi^*$ state with optically "dark" feature, the overall fluorescence emission of the excited BDA-1 is completely suppressed. Notably, our calculations provide a new explanation for the

Fig. 5. Absorption and energy decay processes of $[Zn:BDA-1_{-H+}]^+$ upon photoexcitation, where the left and right panels show MOs involved in the S_0–S_1 transition at the S_0 and S_1 optimized geometry, respectively.

Table 4

The IFCT analyses of the dominant absorption and radiative transitions for BDA-1 and its metal ion complexes, where $\Delta\Theta$ shows the amount of net transferred electron, BDP is the BODIPY fragment, DME is the DME unit, PY is the pyridyl ring, and M is the metal ion.

	transition	$\Delta\Theta_{(BDP-DME)}$	$\Delta\Theta_{(BDP-PY)}$	$\Delta\Theta_{(BDP-M)}$	$\Delta\Theta_{(DME-PY)}$	$\Delta\Theta_{(DME-M)}$	$\Delta\Theta_{(PY-M)}$
BDA-1	$S_0 \to S_1$(abs.)	−0.721	−0.057	–	0.006	–	–
	$S_0 \to S_2$(abs.)	0.135	0.014	–	−0.001	–	–
	$S_0 \leftarrow S_1$(fl.)	−0.775	−0.092	–	−0.009	–	–
	$S_0 \leftarrow S_2$(fl.)	0.136	−0.010	–	−0.003	–	–
$[Zn:BDA-1_{-H+}]^+$	$S_0 \to S_1$(abs.)	0.101	0.303	0.050	0.011	0.001	−0.002
	$S_0 \leftarrow S_1$(fl.)	0.037	0.755	0.024	0.067	0.002	−0.003
$[Cd:BDA-1_{-H+}]^+$	$S_0 \to S_1$(abs.)	0.084	0.215	0.198	0.017	0.015	−0.001
	$S_0 \leftarrow S_1$(fl.)	0.022	0.087	0.572	0.024	0.156	0.001
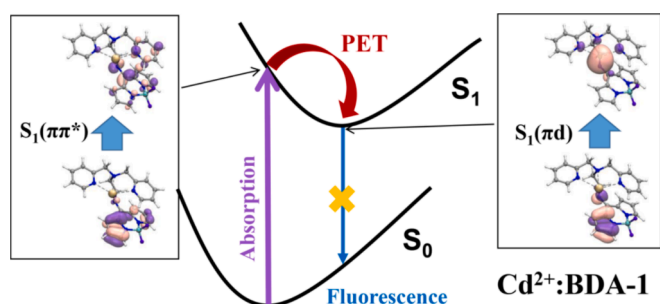
Fig. 6. Absorption and energy decay processes of $[Cd:BDA-1_{-H+}]^+$ upon photoexcitation, where the left and right panels show MOs involved in the S_0–S_1 transition at the S_0 and S_1 optimized geometry, respectively.

weak fluorescence of BDA-1 observed in experiments, which is different from the previously proposed PET mechanism [17].

With the addition of Zn^{2+} or Cd^{2+} ions, the deprotonated BDA-1 can efficiently bind to one metal ion by tetradentate chelating interaction. The absorption and fluorescence emission observed in experiments [17] are both attributed to the S_0–S_1 transition of the metal ion-ligand complexes. Moreover, d-PET process can efficiently occur in these two complexes upon photo-excitation, according to frontier MO analyses. However, as the coordination bond between Cd^{2+} and N(1) atom in the excited $[Cd:BDA-1_{-H+}]^+$ complex is significantly weakened in comparison to that of the $[Zn:BDA-1_{-H+}]^+$ complex in the S_1 state, the MO compositions involved in the $S_1 \to S_0$ radiation are remarkably changed for the two complexes. A charge transfer from the BODIPY fluorophore to the tertiary amine contributes the S_1–S_0 transition in $[Zn:BDA-1_{-H+}]^+$, while the S_1 state of $[Cd:BDA-1_{-H+}]^+$ has typical LMCT features as an optically "dark" state, because of the change of dominant MO component from the hybridized π^* orbitals to the d orbital of Cd^{2+} ion. For comparison, we performed the similar calculations on the BDA-1's performance for detecting Hg^{2+} and Cu^+ ions. The major results involving the optimized geometries, absorption and emission features are listed in Figure S2 and Table S1. To our surprise, the formed metal–ligand complexes show completely different decay mechanisms upon photo-excitation, in which the excited state can rapidly decay to the dark S_1 state by efficient internal conversion. As a result, BDA-1 does not show the fluorescence-enhance effect for Hg^{2+} and Cu^+ either.

In summary, the BDA-1 molecule, as a typical tetradentate chelating probe, exhibits an unusual fluorescence-enhancement mechanism for Zn^{2+} ion. Although the d-PET process is commonly known to have fluorescence inhibiting effect, the forming $[Zn:BDA-1_{-H+}]^+$ complex remains considerable radiative ability. In contrast, with the addition of Cd^{2+}, fluorescence radiation of $[Cd:BDA-1_{-H+}]^+$ is doubly suppressed. The current calculations provide solid evidence and reliable explanation for the zinc ion-specificity of BDA-1 as a so-called fluorescence-enhanced probe.

CRediT authorship contribution statement

Quyan Su: Writing – original draft, Investigation, Formal analysis, Data curation. **Jia Han:** Validation, Methodology, Data curation. **Haili Yu:** Validation, Methodology, Data curation. **Xiaoguo Zhou:** Writing – review & editing, Visualization, Supervision, Project administration, Conceptualization. **Shilin Liu:** Resources, Project administration, Funding acquisition.

Declaration of competing interest

The authors declare that they have no known competing financial interests or personal relationships that could have appeared to influence the work reported in this paper.

Data availability

Data will be made available on request.

Appendix A. Supplementary data

Supplementary data to this article can be found online at https://doi.org/10.1016/j.saa.2024.124854.

Comparison of the current and previously proposed geometries of the BDA-1 molecule in ground state; Optimized geometries of $[Hg:BDA-1_{-H+}]^+$ and $[Cu:BDA-1_{-H+}]$ complexes in the S_0 and S_1 states; Properties of absorption (abs.) and fluorescence (fl.) transitions of the $[Hg:BDA-1_{-H+}]^+$ and $[Cu:BDA-1_{-H+}]$ complexes.

References

[1] J.M. Berg, Y. Shi, The Galvanization of Biology: A Growing Appreciation for the Roles of Zinc, Sci. 271 (1996) 1081–1085, https://doi.org/10.1126/science.271.5252.1081.

[2] E.L. Que, D.W. Domaille, C.J. Chang, Metals in Neurobiology: Probing Their Chemistry and Biology with Molecular Imaging, Chem. Rev. 108 (2008) 1517–1549, https://doi.org/10.1021/cr078203u.

[3] S.D. Portbury, P.A. Adlard, Zinc signal in brain diseases, Int. J. Mol. Sci. 18 (2017) 2506, https://doi.org/10.3390/ijms18122506.

[4] G.A. Naikoo, H. Salim, I.U. Hassan, T. Awan, F. Arshad, M.Z. Pedram, W. Ahmed, A. Qurashi, Recent advances in non-enzymatic glucose sensors based on metal and metal oxide nanostructures for diabetes management-a review, Front. Chem. 9 (2021) 748957, https://doi.org/10.3389/fchem.2021.748957.

[5] A. Inobeme, J.T. Mathew, E. Jatto, J. Inobeme, C.O. Adetunji, M. Muniratu, B. I. Onyeachu, M.A. Adekoya, A.I. Ajai, A. Mann, E. Olori, S.O. Akhor, C.A. Eziukwu, T. Kelani, P.I. Omali, Recent advances in instrumental techniques for heavy metal

quantification, Environ. Monit. Assess. 195 (2023) 452, https://doi.org/10.1007/s10661-023-11058-3.

[6] M. Kumar Goshisht, G. Kumar Patra, N. Tripathi, Fluorescent Schiff base sensors as a versatile tool for metal ion detection: strategies, mechanistic insights, and applications, Materials Advances 3 (2022) 2612–2669, https://doi.org/10.1039/D1MA01175H.

[7] Z. Guo, G.-H. Kim, J. Yoon, I. Shin, Synthesis of a highly Zn2+-selective cyanine-based probe and its use for tracing endogenous zinc ions in cells and organisms, Nat. Protoc. 9 (2014) 1245–1254, https://doi.org/10.1038/nprot.2014.086.

[8] J. Du, K. Chen, Z. Yu, Y. Qiao, J. Liu, Q. Zhai, Z. Hu, S.-G. Yang, J. Li, H. Teng, Development of bi-oligo (ethylene glycol)-functionalized fluorescent probe for two-photon and noninvasive imaging in *Arabidopsis thaliana*, Advanced Agrochem 1 (2022) 162–173, https://doi.org/10.1016/j.aac.2022.11.003.

[9] A. Jiang, Y. Liu, G. Chen, Y. Li, B. Tang, The cross-talk modulation of excited state electron transfer to reduce the false negative background for high fidelity imaging in vivo, Chem. Sci. 11 (2020) 1964–1974, https://doi.org/10.1039/C9SC05765J.

[10] J. Yu, H. Yu, S. Wang, Y. Qi, Progress in research of zinc ion fluorescent probes for biological imaging, J. Lumin. (2023) 120318, https://doi.org/10.1016/j.jlumin.2023.120318.

[11] H. Fang, S. Geng, M. Hao, Q. Chen, M. Liu, C. Liu, Z. Tian, C. Wang, T. Takebe, J.-L. Guan, Simultaneous Zn2+ tracking in multiple organelles using super-resolution morphology-correlated organelle identification in living cells, Nat. Commun. 12 (2021) 109, https://doi.org/10.1038/s41467-020-20309-7.

[12] T. Anand, A.S. Kumar, S.K. Sahoo, A novel Schiff base derivative of pyridoxal for the optical sensing of Zn2+ and cysteine, Photochem. Photobiol. Sci. 17 (2018) 414–422, https://doi.org/10.1039/C7PP00391A.

[13] B. Das, M. Dolai, A. Dhara, A. Ghosh, S. Mabhai, A. Misra, S. Dey, A. Jana, Solvent-regulated fluorimetric differentiation of Al3+ and Zn2+ using an AIE-active single sensor, Chem. A Eur. J. 125 (2021) 1490–1504, https://doi.org/10.1021/acs.jpca.0c10518.

[14] L. Yan, X. Wen, Z. Fan, A large-Stokes-shift fluorescent probe for Zn 2+ based on AIE, and application in live cell imaging, Anal. Bioanal. Chem. 412 (2020) 1453–1463, https://doi.org/10.1007/s00216-019-02378-w.

[15] Y. Mikata, M. Tanaka, S. Yasuda, A. Tsuruta, T. Hagiwara, H. Konno, T. Matsuo, Effect of methoxy substituents on fluorescent Zn 2+/Cd 2+ selectivity of bisquinoline derivatives with a N, N′-dimethylalkanediamine skeleton, Dalton Trans. (2023), https://doi.org/10.1039/D3DT00597F.

[16] S. Paul, P. Banerjee, An ESIPT based turn on fluorochromogenic sensor for low level discrimination of chemically analogous Zn2+ and Cd2+ & aqueous phase recognition of bio-hazardous CN-: from solution state analysis to prototype fabrication, Sens. Actuators B 329 (2021) 129172.

[17] X. Chen, W. Niu, Q. Yuan, Y. Zhang, X. Gao, D. Su, Mapping the endogenous Zn2+ in situ during zebrafish embryogenesis by a fluorogenic sensor, Sens. Actuators B 376 (2023) 132937, https://doi.org/10.1016/j.snb.2022.132937.

[18] T. Lu, molclus program, Version 1.9.9.6, (2021). http://www.keinsci.com/research/molclus.html (accessed February 24, 2022).

[19] C. Bannwarth, S. Ehlert, S. Grimme, GFN2-xTB—An accurate and broadly parametrized self-consistent tight-binding quantum chemical method with multipole electrostatics and density-dependent dispersion contributions, J. Chem. Theory Comput. 15 (2019) 1652–1671, https://doi.org/10.1021/acs.jctc.8b01176.

[20] S. Grimme, C. Bannwarth, P. Shushkov, A robust and accurate tight-binding quantum chemical method for structures, vibrational frequencies, and noncovalent interactions of large molecular systems parametrized for all spd-block elements (Z= 1–86), J. Chem. Theory Comput. 13 (2017) 1989–2009, https://doi.org/10.1021/acs.jctc.7b00118.

[21] M.J. Frisch, G.W. Trucks, H.B. Schlegel, G.E. Scuseria, M.A. Robb, J.R. Cheeseman, G. Scalmani, V. Barone, G.A. Petersson, H. Nakatsuji, GAUSSIAN16. Revision A. 03. Gaussian Inc., Wallingford, CT, USA, 2016.

[22] R.E. Stratmann, J.C. Burant, G.E. Scuseria, M.J. Frisch, Improving harmonic vibrational frequencies calculations in density functional theory, J. Chem. Phys. 106 (1997) 10175–10183, https://doi.org/10.1063/1.474047.

[23] E. Runge, E.K. Gross, Density-functional theory for time-dependent systems, Phys. Rev. Lett. 52 (1984) 997, https://doi.org/10.1103/PhysRevLett.52.997.

[24] P.J. Stephens, F.J. Devlin, C.F. Chabalowski, M.J. Frisch, Ab initio calculation of vibrational absorption and circular dichroism spectra using density functional force fields, J. Phys. Chem. 98 (1994) 11623–11627, https://doi.org/10.1021/j100096a001.

[25] M.M. Francl, W.J. Pietro, W.J. Hehre, J.S. Binkley, M.S. Gordon, D.J. DeFrees, J. A. Pople, Self-consistent molecular orbital methods. XXIII. A polarization-type basis set for second-row elements, J. Chem. Phys. 77 (1982) 3654–3665, https://doi.org/10.1063/1.444267.

[26] P.J. Hay, W.R. Wadt, Ab initio effective core potentials for molecular calculations, Potentials for the Transition Metal Atoms Sc to Hg, the Journal of Chemical Physics 82 (1985) 270–283, https://doi.org/10.1063/1.448799.

[27] S. Grimme, J. Antony, S. Ehrlich, H. Krieg, A consistent and accurate ab initio parametrization of density functional dispersion correction (DFT-D) for the 94 elements H-Pu, J. Chem. Phys. 132 (2010) 154104, https://doi.org/10.1063/1.3382344.

[28] M.F. Iozzi, B. Mennucci, J. Tomasi, R. Cammi, Excitation energy transfer (EET) between molecules in condensed matter: A novel application of the polarizable continuum model (PCM), J. Chem. Phys. 120 (2004) 7029–7040, https://doi.org/10.1063/1.1669389.

[29] T. Lu, F. Chen, Multiwfn: A multifunctional wavefunction analyzer, J. Comput. Chem. 33 (2012) 580–592, https://doi.org/10.1002/jcc.22885.

[30] V.G. Tsirelson, A. Stash, Analyzing experimental electron density with the localized-orbital locator, Acta Crystallogr. B 58 (2002) 780–785, https://doi.org/10.1107/s0108768102012338.

[31] T. Lu, F. Chen, Bond Order Analysis Based on the Laplacian of Electron Density in Fuzzy Overlap Space, Chem. A Eur. J. 117 (2013) 3100–3108, https://doi.org/10.1021/jp4010345.

[32] P. Klán, J. Wirz, Photochemistry of organic compounds: from concepts to practice, John Wiley & Sons (2009) 35–37.